The Astronomical Journal, 166:144 (13pp), 2023 October https://doi.org/10.3847/1538-3881/aced8e

Timescale of Stellar Feedback-driven Turbulence in the ISM: A Deep Dive into UGC 4305

Laura Congreve Hunter[1], Liese van Zee[1], Kristen B. W. McQuinn[2], Roger E. Cohen[2], Madison Markham[1,3], and Andrew E. Dolphin[4,5]
[1] Department of Astronomy, Indiana University, 727 East 3rd Street, Bloomington, IN 47405, USA
[2] Rutgers University, Department of Physics and Astronomy, 136 Frelinghuysen Road, Piscataway, NJ 08854, USA
[3] Colgate University, Department of Physics and Astronomy, Ho Science Center, Oak Drive East Extension, Hamilton, NY 13346, USA
[4] Raytheon Technologies, 1151 E. Hermans Road, Tucson, AZ 85756, USA
[5] University of Arizona, Steward Observatory, 933 North Cherry Avenue, Tucson, AZ 85721, USA
Received 2023 May 16; revised 2023 August 2; accepted 2023 August 3; published 2023 September 5

Abstract

Understanding the interplay of stellar feedback and turbulence in the interstellar medium (ISM) is essential to modeling the evolution of galaxies. To determine the timescales over which stellar feedback drives turbulence in the ISM, we performed a spatially resolved, multiwavelength study of the nearby star-forming dwarf galaxy UGC 4305. As indicators of turbulence on local scales (400 pc), we utilized ionized gas velocity dispersion derived from IFU Hα observations and atomic gas velocity dispersion and energy surface densities derived from H I synthesis observations with the Very Large Array. These indicators of turbulence were tested against star formation histories over the past 560 Myr derived from color–magnitude diagrams using Spearman's rank correlation coefficient. The strongest correlation identified at the 400 pc scale is between measures of H I turbulence and star formation 70–140 Myr ago. We repeated our analysis of UGC 4305's current turbulence and past star formation activity on multiple physical scales ($\sim$560 and 800 pc) to determine whether there are indications of changes in the correlation timescale with changes to the physical scale. No notable correlations were found at larger physical scales, emphasizing the importance of analyzing star formation-driven turbulence as a local phenomenon.

Unified Astronomy Thesaurus concepts: Interstellar medium (847); Dwarf galaxies (416); Extragalactic astronomy (506); Radio astronomy (1338); Interstellar atomic gas (833); Optical astronomy (1776)

1. Introduction

Stellar feedback-driven turbulence in the interstellar medium (ISM) is a key process impacting the evolution of galaxies. This interplay between star formation and the ISM is invoked to explain the observed properties of galaxies such as the mass–metallicity relationship (e.g., Tremonti et al. 2004; Brooks et al. 2007; Christensen et al. 2018) and the dark matter distribution of dwarf galaxies (Bullock & Boylan-Kolchin 2017). Stellar feedback, from supernovae (SNe), ionizing radiation of high-mass stars, and stellar winds from evolved stars (e.g., Spitzer 1978; Elmegreen & Scalo 2004; Mac Low & Klessen 2004), input energy into the ISM, altering its distribution and increasing its kinetic energy and turbulence. This relationship has been observed for the ionized gas (Moiseev et al. 2015; Yu et al. 2019) and atomic gas at high star formation rate (SFR) surface densities (e.g, Joung et al. 2009; Tamburro et al. 2009; Stilp et al. 2013a) as a correlation between current star formation activity and measures of the ISM's turbulence.

Much of the previous observational work to correlate ISM turbulence and star formation has utilized integrated light techniques with set timescales ($<$10 Myr for Hα and $<$100 Myr for the far UV; see Kennicutt & Evans 2012 and references therein) to determine star formation rates (e.g, Elmegreen & Scalo 2004; Zhou et al. 2017; Hunter et al. 2021). These integrated light techniques, however, do not account for the time variability of galaxies' star formation histories (SFHs) (e.g, Dolphin et al. 2005; McQuinn et al. 2010a, 2010b; Weisz et al. 2011, 2014). To account for this established variability, time-resolved star formation activity can be reconstructed using fitting techniques with color–magnitude diagrams (CMDs; e.g, Tolstoy & Saha 1996; Dolphin 1997; Holtzman et al. 1999; Harris & Zaritsky 2001; Aparicio & Hidalgo 2009). It has been demonstrated that these time-resolved SFHs provide the necessary tools to determine whether past stellar feedback drives the current ISM turbulence (e.g, Stilp et al. 2013c; Hunter et al. 2022). From the analysis of a sample of 18 dwarf galaxies, Stilp et al. (2013c) identified strong indications that the globally averaged H I turbulence, measured by H I kinetic energy, and star formation activity 30–40 Myr ago, from CMD-derived SFHs, are correlated. Looking into the spatially resolved properties of four dwarf galaxies, Hunter et al. (2022) found evidence of a correlation between turbulence in the atomic gas and star formation 100–200 Myr ago on local scales ($\sim$400 pc). Additionally, Hunter et al. (2022) found no evidence of a correlation at the 30–40 Myr timescale on local scales. This observed difference in correlation timescale may indicate that there are physical differences in the turbulence properties at global and local scales.

This paper focuses on analysis of a single galaxy, UGC 4305, to explore further effects of spatial and time resolution because, in Hunter et al. (2022), the finer spatial resolution prevented the use of SFHs with time resolution comparable to the 10 Myr resolution used in Stilp et al. (2013c). The difference in the correlation timescales found in the two papers may be related to the differences in methodology. By focusing on a single, nearby, star-forming galaxy, finer time binning can

be used for the SFHs to better match the time resolution of Stilp et al. (2013c). A finer time resolution can be applied for a single galaxy because the systematic uncertainties in the SFH may not come into play when doing a relative comparison of different regions within a single galaxy. For this analysis, we can treat the statistical uncertainties as the relevant errors. By eliminating the effects of differences in time binning on the results, we can confirm that the difference in timescale is driven by differences in the global and local turbulence properties.

UGC 4305, also known as Holmberg II, is a nearby dwarf galaxy at a distance of 3.38 ± 0.05 Mpc (Tully et al. 2013), with a stellar mass of $\log(M_{*r}/M_{\odot}) = 8.48$ (McQuinn et al. 2019), Hα-derived SFR of -1.44 ± 0.05 $\log(M_{\odot})$ yr^{-1}, and absolute B-band magnitude of -16.06 ± 0.04 (McQuinn et al. 2019). UGC 4305 has an intriguing atomic gas distribution with a distinct flocculent spiral structure seen in the central regions and a comet-like structure in the outermost regions (Bureau & Carignan 2002). Across its disk are a large number of well documented H I holes ranging in sizes from $\sim$100 pc to nearly 2 kpc with expansion velocities from 3 to 18 km s^{-1} (e.g., Puche et al. 1992; Bagetakos et al. 2011; Pokhrel et al. 2020). The largest of these holes represent the displacement of $\sim$5% of the total H I mass of the galaxy and have dynamical ages in the range of 70–150 Myr (Pokhrel et al. 2020). These giant H I cavities were explained by Puche et al. (1992) as being created through multiple SNe and stellar winds from massive stars formed contemporaneously in the same location. This origin of the H I holes was tested against the holes' characteristics and stellar populations by Rhode et al. (1999), Bureau & Carignan (2002), and Weisz et al. (2009). It was found that many H I holes lacked the required single stellar populations for SNe to drive such large shells (Rhode et al. 1999). Alternative methods to create the observed structures have been proposed including ram pressure stripping, and thermal and gravitational instabilities (Bureau & Carignan 2002; Dib & Burkert 2005). Weisz et al. (2009) and Bagetakos et al. (2011) demonstrated that these structures contain multiple generations of stars and that the energy input over multiple past star formation events could form the H I holes observed.

The complex structures of the atomic gas are continued in the ionized gas with a mixture of high-surface-brightness and diffuse Hα features. One of the notable regions with broad Hα features in the southeast of the galaxy is the well known ultraluminous X-ray source Holmberg II X-1, discovered in the ROSAT All-Sky Survey (Moran et al. 1996) and believed to be an X-ray binary with extensive multiwavelength analysis (e.g., Zezas et al. 1999; Kaaret et al. 2004; Miller et al. 2005; Berghea et al. 2010; Egorov et al. 2017a). The bulk distribution and kinematics of the ionized gas have been subject to careful analysis of the shells and bubble structures and compared to the mapping of the neutral gas structure (e.g., Hunter et al. 1993; Hodge et al. 1994; Stewart et al. 2000; Egorov et al. 2017b; McQuinn et al. 2019). The ionized gas is overall found to contain a handful of very prominent Hα supershells and a larger number of fainter expanding superbubbles with extensive diffuse gas filling in some of the H I holes across the disk of the galaxy (Hunter et al. 1993; Egorov et al. 2017b; McQuinn et al. 2019).

The stellar populations of the high-surface-brightness inner regions have had multiple CMD-derived star formation histories (e.g., Weisz et al. 2008; McQuinn et al. 2010a; Dalcanton et al. 2012; Cignoni et al. 2018) from IR, optical, and UV observations, which agree in the shape of the SFH over the past few hundred million years. These SFHs show continuous star formation over the past 500 Myr on the scale of 2.2×10^{-2} $M_{\odot}$ yr^{-1} (HST UV, Cignoni et al. 2018) to 6×10^{-2} $M_{\odot}$ yr^{-1} (optical, Weisz et al. 2008; McQuinn et al. 2010a), with an increase in star formation rate by a factor of 1.5 to 2 in the recent past ($\leqslant$30 Myr) compared to the past few hundred million years (Dalcanton et al. 2012; Cignoni et al. 2018). Explanations for this ongoing star formation include proposed internal processes such as SNe and shocks triggering the collapse of nearby gas clouds and resulting in new star formation (Stewart et al. 2000). In support of internal mechanisms, Egorov et al. (2017b) proposes that the most recent round of star formation was triggered by a collision between the wall of the most extended (2 kpc) H I shell in the galaxy and other H I structures located to the north of the shell. Conversely, a theory of ram pressure stripping by the intergalactic medium possibly triggering recent star formation is presented in Bernard et al. (2012)'s analysis of UGC 4305's full stellar disk and comet-like extended H I disk.

In this paper, we focus on the correlation timescale of the neutral and ionized gas kinematics of the galaxy UGC 4305. Section 2 presents the data used from the Very Large Array (VLA[6]), Hubble Space Telescope (HST), and WIYN[7] 3.5 m telescope, and Section 3 explains how SFHs are derived and the turbulence of the ionized and atomic gas is measured. Section 4 presents our Hα results, Section 5 presents our results for the H I and discusses the relation between timescale and the physical scale in the atomic gas, and Section 6 summarizes the results and conclusions.

2. Observational Data

For this analysis, new and archival multiwavelength observations have been processed. Archival radio synthesis observations by the VLA of the 21 cm neutral hydrogen line are used to determine the velocity dispersions and energy surface densities of the atomic gas. SFHs were derived from CMDs of archival F555W and F814W HST observations of resolved stars. Ionized gas kinematics were provided by observations with the integral field unit (IFU) SparsePak on the WIYN 3.5 m telescope.

UGC 4305 was selected for study as it has a large enough stellar disk with a diameter of the isophote where the surface brightness is 25 mag/arcsec^2 of $375\farcs8$, or approximately 6.2 kpc (McQuinn et al. 2019), and sufficient HST coverage to yield 125 regions, enough for an independent analysis. This ability to analyze the galaxy as an individual allows the use of finer time resolution to probe the 100–200 Myr timescale identified by Hunter et al. (2022) and the 30–40 Myr timescale identified by Stilp et al. (2013c). When comparing between regions within the same galaxy the systematic uncertainties are less relevant and the errors are dominated by the smaller statistical uncertainties. Additionally, UGC 4305 was chosen as it is nearly face-on, with an eccentricity of 0.72 (McQuinn et al.

[6] The VLA is operated by the NRAO, which is a facility of the National Science Foundation operated under cooperative agreement by Associated Universities, Inc.

[7] The WIYN Observatory is a joint facility of the NSF's National Optical–Infrared Astronomy Research Laboratory, Indiana University, the University of Wisconsin–Madison, Pennsylvania State University, the University of Missouri, the University of California–Irvine, and Purdue University.

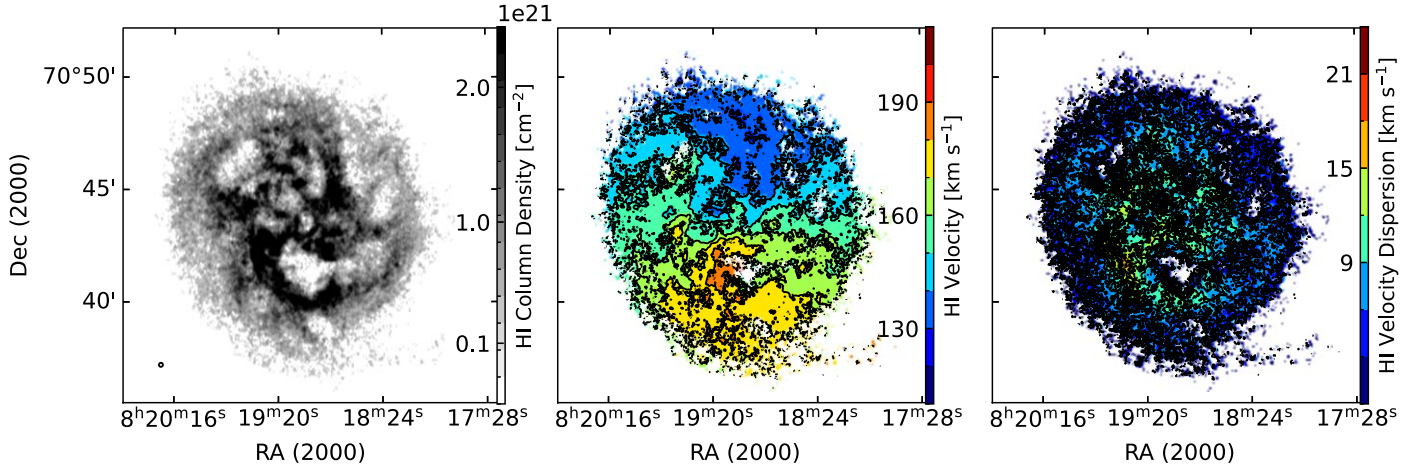

Figure 1. The VLA-derived H I moment maps of UGC 4305. Left: H I zeroth moment map (column density) in units of 10^{21} H atoms cm^{-2}; center: H I first moment map (velocity field) with isovelocity contours spaced every 10 km s^{-1}; right: H I second moment map (velocity dispersion) with isovelocity contours at 3 km s^{-1} spacing. In the bottom left of the first panel is the beam size ($10\farcs73 \times 10\farcs40$) of the H I data cube used.

2019). Face-on is the ideal geometry for turbulence studies as it limits the effects of line broadening due to rotation and means we are not looking through a larger volume than necessary.

2.1. VLA Observations

Archival observations with the VLA in B, C, and D configurations from the observing program AP196 (PI D. Puche) were used. For this study, the archival data were reprocessed in AIPS[8] to match the handling of the sample in Hunter et al. (2022). After correcting for Doppler shifts between observing blocks and continuum subtraction, the observing blocks were combined and a uvtaper of 40 40 and uvrange 0 50 along with a robust of 5 were chosen when creating the final data cube using the AIPS task IMAGR. The tapering was chosen to increase sensitivity at the expense of some spatial resolution. The final data cube had a velocity resolution of 2.58 km s^{-1}, rms = 1.047 mJy beam^{-1}, and beam of $10\farcs73 \times 10\farcs40$ with a position angle of $-0.9°$. We recovered a total H I flux of 220 ± 22 Jy km s^{-1} or H I mass given by $\log(\text{H I mass}/M_\odot) = 8.77 \pm 0.05$. The final beam size was such that each region of interest contained multiple resolution elements. The resulting zeroth, first, and second moment maps are presented in Figure 1.

2.2. Archival HST Observations

CMDs derived from HST imaging of resolved stellar populations taken with the Advanced Camera for Survey (ACS, Ford et al. 1998) for Project ID 10605 (PI E. Skillman) were used to determine the SFHs. Two pointings with 4660 s exposures were taken with ACS's F555W *V* filter and F814W *I* filter. The ACS instrument has a pixel scale of $0\farcs05$ and a $202'' \times 202''$ field of view (FoV). The optical imaging, summarized here, was processed to match Hunter et al. (2022) and in the manner described in STARBIRDS (McQuinn et al. 2015). For a detailed description of the data reduction, we refer the reader to McQuinn et al. (2010b). The software DOLPHOT, optimized for the ACS instrument (Dolphin 2000, 2016), was used to perform photometry on the pipeline-processed images after correction for charge transfer efficiency. As in STARBIRDS, the photometry was filtered to include well-recovered point sources, and the same quality cuts on signal-to-noise ratios (S/Ns), crowding conditions, and sharpness parameters were applied. To measure the completeness function of the stellar catalogs, we ran ∼5 million artificial star tests over each ACS field of view. The artificial star tests were run on the individual images. The ∼5 million ASTs per FoV ensured sufficient numbers of stars per $24'' \times 24''$ region of interest.

2.3. SparsePak Observations

The SparsePak IFU (Bershady et al. 2004) on the WIYN 3.5 m telescope was used for spatially resolved spectroscopy of the ionized gas on 2021 December 6, 7, 10, and 11 and 2023 January 21 and February 11 and 12. In total, 16 SparsePak fields were observed to cover the majority of the high-surface-brightness areas and much of the diffuse ionized gas of the galaxy. The SparsePak IFU has 82 fibers with a $4\farcs69$ diameter arranged in a fixed $70'' \times 70''$ square. In the core, fibers are adjacent while they are separated by $11''$ in the rest of the field. The same setup for the bench spectrograph was used for all observations, including the 316@63.4 grating, X19 blocking filter and observing at order 8 for velocity resolution of 13.9 km s^{-1} pixel^{-1} and wavelength range of 6480 to 6890 Å, centered on 6683.933 Å. For 12 of the 16 pointings, a three-pointing dither pattern was used to fill in the gaps between fibers. For the remainder, only a single pointing was observed. For the majority of pointings, three exposures of 780 s were taken to detect both the diffuse ionized gas and bright Hα knots. To remove telluric line contamination, observations were taken of nearby patches of blank sky, as the galaxy extended well beyond the SparsePak field of view.

As in Hunter et al. (2022), the standard tasks in the IRAF[9] HYDRA package were used to process the SparsePak data. The blank sky observations were used to sky-subtract the individual images and a customized Python sky subtraction routine to remove sky line residuals. After sky subtraction, to increase the S/N, the three exposures were averaged together. The reduced

[8] The Astronomical Image Processing System (AIPS) was developed by the NRAO.

[9] IRAF is distributed by NOAO, which is operated by the Association of Universities for Research in Astronomy, Inc., under cooperative agreement with the National Science Foundation.

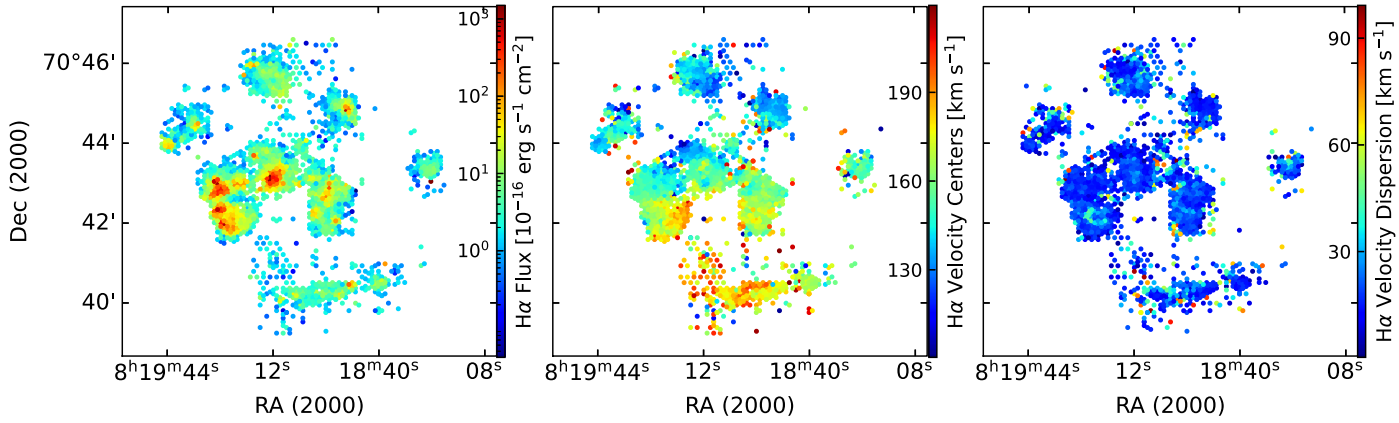

Figure 2. SparsePak IFU (WIYN 3.5 m) map of UGC 4305, with Hα line measurements from PAN and FXCOR. Left: Hα flux on a logarithmic scale in units of 10^{-16} erg s^{-1} cm^{-1}; center: Hα recessional velocities; right: map of Hα velocity dispersion ($\sigma_{\rm H\alpha}$). Each filled circle corresponds to a fiber's size and position on the sky. See Figure 4 for where the Sparsepak fibers fall compared to UGC 4305's H I and optical distributions.

spectra of the galaxy were smoothed by a Gaussian with a sigma of 1 pixel (0.306 Å) in order to reduce the noise. Peak Analysis (PAN; Dimeo 2005, an IDL software suite) was used to fit a Gaussian to each fiber spectrum. The recessional velocity of each emission line was determined using FXCOR in IRAF. The measured FWHMs of the Hα line were corrected for instrumental broadening of 48.5 km s^{-1}, as measured from the equivalently smoothed ThAr spectra. The measured FWHMs are then converted to $\sigma_{\rm H\alpha}$ for the analysis using $\sigma = {\rm FWHM}/\sqrt{8\ln(2)}$. The H$\alpha$ line measurements (fluxes, centers, and velocity dispersions) from PAN were visually inspected and fibers that passed were mapped to their SparsePak fiber location. The PAN line fluxes and velocity dispersions are shown in Figure 2 along with the velocity field determined by FXCOR.

3. Methods

As in Hunter et al. (2022), UGC 4305 was divided into 400 × 400 regions to study the impact of stellar feedback at a spatially resolved scale. Each region has an independently measured SFH, and individual ionized and atomic gas velocity dispersions. We chose to partition UGC 4305 into square regions 400 × 400 pc (24″ by 24″) in size as a balance of our observational limits and expectations from theory. As described in Hunter et al. (2022), the largest reasonable scale for the analysis was determined to be 400 pc. Four hundred parsecs is on the scale of individual and clustered SNe (superbubbles) yet large enough to have sufficient star counts for resolved star formation histories. In addition, momentum from superbubbles is driven into the ISM at scales up to a few times the galaxy's disk thickness (Kim et al. 2017; Gentry et al. 2017). For dwarf galaxies this is roughly 200 to 600 pc (Bacchini et al. 2020). Thus, larger region sizes are not expected to be as sensitive to the impacts on the ISM of local, as compared to global, star formation activity (see also Section 5.1).

3.1. Star Formation Histories

As in Hunter et al. (2022), the SFHs were reconstructed from resolved stellar populations using MATCH, a numerical CMD fitting program (Dolphin 2002). For a complete description of the methods see McQuinn et al. (2010b). In brief, MATCH uses a stellar evolution library (PARSEC stellar library, Bressan et al. 2012) and assumed initial mass function (Kroupa 2001) to create synthetic simple stellar populations with a range of ages and metallicities. In this work, an assumed binary fraction of 35% with a flat distribution of binary mass ratio was implemented for the SFH solutions. No internal differential extinction was assumed due to the low metallicity of UGC 4305 ($\log({\rm O/H}) + 12 = 7.92 \pm 0.10$, Croxall et al. 2009). For the foreground extinction, the Schlafly & Finkbeiner (2011) recalibration of the Schlegel et al. (1998) dust emission maps was used with all regions having the same foreground extinction correction. The completeness, photometric bias, and photometric scatter measured from the artificial star tests are used to simulate the observational errors (from photon noise and blending). To calculate the expected stellar distribution of any SFH on a CMD, the synthetic CMDs were combined linearly along with simulated CMDs of foreground stars.

The likelihood that an observed V versus $(V - I)$ CMD was produced by the SFH of a particular synthetic CMD was calculated and the SFH most likely to produce the observed data for each region was determined using a maximum likelihood algorithm. A hybrid Markov Chain Monte Carlo simulation was used to estimate the random uncertainties (Dolphin 2013). These statistical uncertainties are the relevant uncertainties to consider for our inter-region comparison within an individual galaxy. We adopt a time binning for the SFH of $\Delta\log(t) = 0.15$ over the most recent 560 Myr, which more than covers the timescales of interest for star formation-driven turbulence. Example CMDs and the resulting SFHs for a region in UGC 4305 are shown in Figure 3. The median number of observed stars per region was 3182, while the minimum was 201 and the maximum 7929.

In Hunter et al. (2022), regions were only included if they contained sufficient numbers of blue stars (>50) in the upper main sequence, which helped ensure robustly determined recent SFRs. These blue stars have an F555W – F814W color <0.4 and a magnitude F814W <26. Working with the larger number of regions for UGC 4305, it was found that making such cuts could exclude regions with no current star formation but with star formation in the past 500 Myr. Such a cut could bias us toward shorter correlation timescales, as only regions with recent star formation would be included. For UGC 4305, the median number of blue stars per region was 182; the fewest blue stars in a region was 12 and the region with the most had 752. Thus, for the results presented in this paper, we

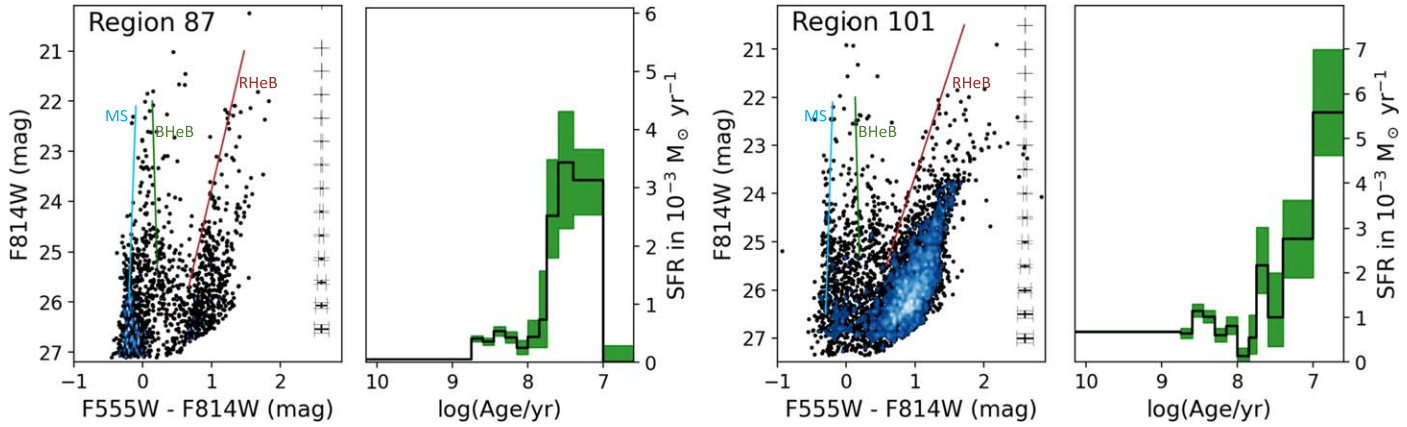

Figure 3. Example CMD and SFH for two 400 × 400 pc regions in UGC 4305 from ACS data. The main sequence (blue), blue helium-burning stars (HeB; green), and red HeB (red) sequences are traced. The SFHs have ⩽15 Myr time resolution in the $t < 70$ Myr time bins with $\Delta\log(t) = 0.15$ time steps and cover the 560 Myr baseline necessary for our science goals. The green shading represents the random uncertainties. To determine the timescales of stellar feedback, each region's CMD-derived SFH is compared with its H I and Hα turbulence measures.

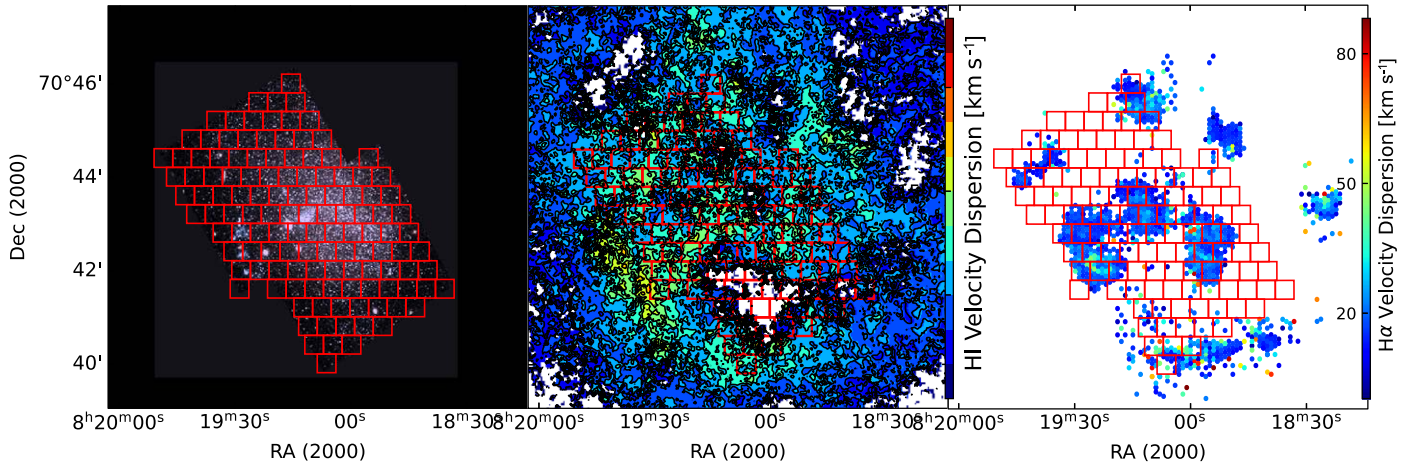

Figure 4. UGC 4305. Left: two-color image from HST observations with ACS where the F814W image is mapped to red and the F555W image is mapped to blue. Center: the VLA H I dispersion map with isovelocity contours at a step size of 3 km s^{-1}. Right: the WIYN 3.5 m SparsePak IFU $\sigma_{H\alpha}$ map. In the right panel, each filled circle represents a fiber's size and position on the sky. Overlaid in red are the outlines of regions used for the analysis.

include all regions, regardless of how well populated the upper main sequence was found to be.

3.2. H I Turbulence Measures

The methods for determining the H I turbulence measures follow those detailed in Hunter et al. (2022) based on the work done in Stilp et al. (2013c) and Ianjamasimanana et al. (2012). We partitioned UGC 4305 into square regions with ∼400 pc per side (24″) with region placements shown in Figure 4. For the H I, velocity dispersions of the regions were measured from the moment maps and by coadding the rotation-corrected line-of-sight profiles. Each region's H I column-density-weighted velocity dispersion of the second moment map was calculated:

$$\sigma_{\rm m2} = \frac{\Sigma_i \sigma_i N_{\rm H\,I,i}}{\Sigma_i N_{\rm H\,I,i}} \quad (1)$$

where $N_{\rm H\,I,i}$ is the H I column density and σ_i is the second-moment velocity dispersion of each pixel. Representative values for the second-moment velocity dispersions are listed in Table 1 with the standard deviation of a weighted average as the uncertainty.

Table 1
UGC 4305 Turbulence Measures

Measure	Units	Median	Range 25%	Range 75%
$\sigma_{H\alpha}$	km s^{-1}	18.1	16.4	19.8
$\sigma_{\rm m2}$	km s^{-1}	10.0	9.1	11.2
$\Sigma_{\rm E,m2}$	10^{51} erg kpc^{-2}	50	33	71
$\sigma_{\rm central}$	km s^{-1}	11.3	10.0	13.6
$\Sigma_{\rm E,central}$	10^{51} erg kpc^{-2}	46	33	67
$\sigma_{\rm wings}$	km s^{-1}	29.8	25.6	34.0
$\Sigma_{\rm E,wings}$	10^{51} erg kpc^{-2}	54	32	84

Notes. $\sigma_{H\alpha}$ is the Hα velocity dispersion.
$\sigma_{\rm m2}$ is the velocity dispersion from the second moment maps and $\Sigma_{\rm E,m2}$ is the corresponding H I energy surface density.
$\sigma_{\rm central}$ is the velocity dispersion from the central superprofile fits and $\Sigma_{\rm E,central}$ is the corresponding H I energy surface density.
$\sigma_{\rm wings}$ is the velocity dispersion from the wings of the superprofile fit and $\Sigma_{\rm E,wings}$ is the corresponding H I energy surface density.

Superprofiles—coadded, line-of-sight H I flux profiles corrected for rotational velocities—were constructed for each region using techniques described in Hunter et al. (2022) to

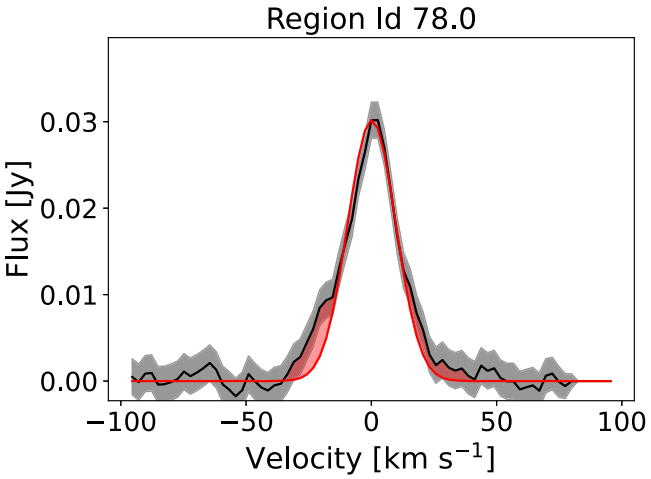

Figure 5. A representative superprofile for a region in UGC 4305. The black line is the H I flux of the region corrected for rotational broadening and the Gaussian fit is shown in red. The error on the data is shaded gray, while wings of the H I profile are shaded red. The wings represent the high-velocity, low-density gas that a single Gaussian does not fit.

determine the velocity dispersion (example: Figure 5). However, in this work, a Python script was used to fit a Gaussian–Hermite function to the line profile to determine the line center to better moderate the fits for lower-S/N locations. Regions were excluded from the H I turbulence analysis if less than one-third of the region has H I flux above the 3σ level. This cut is to ensure only regions with reliable velocity dispersions and H I masses are included. This cut removes 26 of the total 125 regions from the analysis of the atomic gas timescales. The uncertainty of each point in the superprofiles is defined as

$$\sigma = \sigma_{\rm ch,rms} \times \sqrt{N_{\rm pix}/N_{\rm pix/beam}} \quad (2)$$

where $\sigma_{\rm ch,rms}$ is the mean rms noise per channel, $N_{\rm pix}$ is the number of pixels per point of the superprofile, and $N_{\rm pix/beam}$ is the number of pixels per beam or profiles per resolution element. For each superprofile, a Gaussian was scaled to the amplitude and the FWHM of the line profile. The wings of the superprofile seen Figure 5 are the high-velocity, low-density H I flux that is above the Gaussian fit to the superprofile. From the scaled Gaussian fits three parameters were measured:

1. $\sigma_{\rm central}$: σ of the Gaussian profile scaled to the observed H I superprofile's FWHM and amplitude.
2. $f_{\rm wings}$: the fraction of H I in the wings of the superprofile.
3. $\sigma^2_{\rm wings}$: the rms velocity of the wings of the H I profile.

As detailed in Hunter et al. (2022), we estimated the errors of the superprofile fits by adding Gaussian noise using Equation (2) to each point and refitting the superprofiles 2000 times. Examples of $\sigma_{\rm cen}$ and $\sigma_{\rm wing}$, along with $\sigma_{\rm mom2}$, are listed in Table 1 to provide the range of values determined. As a region's velocity dispersion may not be ideal for comparison with the SFH, the H I energy surface density ($\Sigma_{\rm H\,I}$) was determined for each region to account for the H I mass within. The impact of column densities between regions means two regions with the same velocity dispersion may have very different H I energy surface densities. For each velocity dispersion measure, a $\Sigma_{\rm H\,I}$ was estimated using $M_{\rm H\,I}/A_{\rm H\,I}$, the average H I surface density of the region, where $M_{\rm H\,I}$ is the H I mass within the region and $A_{\rm H\,I}$ is the area of the region. The equations for $\Sigma_{\rm H\,I}$ are:

1. $\Sigma_{\rm E,m2}$ is the H I energy surface density from the second moment averages ($\sigma_{\rm m2}$):

$$\Sigma_{\rm E,m2} = \frac{3M_{\rm H\,I}}{2A_{\rm H\,I}}\sigma^2_{\rm m2}. \quad (3)$$

   The 3/2 factor assumes isotropic velocity dispersions and accounts for three-dimensional motion.
2. $\Sigma_{\rm E,central}$ is the H I energy surface density derived from the superprofiles ($\sigma_{\rm central}$):

$$\Sigma_{\rm E,central} = \frac{3M_{\rm H\,I}}{2A_{\rm H\,I}}(1-f_{\rm wing})(1-f_{\rm cold})\sigma^2_{\rm central}. \quad (4)$$

   $M_{\rm H\,I}$ is the total H I mass within the region, $M_{\rm H\,I}(1-f_{\rm wing})(1-f_{\rm cold})$ is the total H I mass contained within the central peak corrected for the dynamically cold H I ($f_{\rm cold}$, $\sigma < 6\,{\rm km\,s^{-1}}$), which $\sigma_{\rm central}$ does not describe well, and the fraction of H I within the wings of the superprofile. As in Hunter et al. (2022) we chose $f_{\rm cold} = 0.15$ to be consistent with Stilp et al. (2013b) and previous estimates for dwarf galaxies (Young et al. 2003; Bolatto et al. 2011; Warren et al. 2012).
3. $\Sigma_{\rm E,wing}$ is the H I energy surface density derived from the wings of the superprofiles ($\sigma_{\rm wing}$):

$$\Sigma_{\rm E,wing} = \frac{3M_{\rm H\,I}}{2A_{\rm H\,I}}f_{\rm wing}\,\sigma^2_{\rm wing}. \quad (5)$$

As in Hunter et al. (2022), a 10% uncertainty is assumed for the H I surface density ($M_{\rm H\,I}/A_{\rm H\,I}$) based on the discussion of the accuracy of measuring H I fluxes in van Zee et al. (1997), and the impact of single-dish versus VLA observations of H I fluxes and masses.

3.3. Measurements of Ionized Gas Turbulence

To better quantify the turbulence in the ionized gas, a different measure for the FWHM was implemented compared to the methods described in Hunter et al. (2022). To determine the turbulence in the ionized gas for each region, the SparsePak fibers were visually inspected and those with clear and distinct Hα line profiles (S/N above ~10) that fell in the region were stacked. A fiber was considered within a region if the central coordinates of the fiber pointing were within the bounds of the region. To remove the bulk motions seen in the Hα velocity fields (central part of Figure 2), the line centers measured from PAN were used to offset all Hα lines to the same center in pixel space. Afterwards, the lines were added together and a third-order polynomial was fit to the continuum and subtracted. The FWHM of the stacked line was measured, taking into consideration whether a line had a single or double peak. The FWHM was corrected for instrumental broadening and was then converted to the velocity dispersion, resulting in $\sigma_{\rm H\alpha}$. The uncertainty of $\sigma_{\rm H\alpha}$ is based on the strength and the narrowness of the line. The S/N of the stacked profiles was calculated with the signal taken as the peak of the stacked line and the noise as the noise of individual fiber spectrum ($\rm Noise_{spec}$, 1.8×10^{-17} erg s^{-1} cm^{-2} Å^{-1}) divided by the square root of the number of fibers ($\rm Num_{fiber}$) included in the

stacked line profile:

$$\frac{\mathrm{S}}{\mathrm{N}} = \mathrm{Peak} \Big/ \left(\frac{\mathrm{Noise_{spec}}}{\sqrt{\mathrm{Num_{fiber}}}} \right). \quad (6)$$

For the uncertainty on the line strength, an S/N of 10 was set to correspond to 10% of peak strength uncertainty and an S/N of 100 to 1% of peak strength uncertainty. For lines with S/N greater than 100 the uncertainty was set to $\frac{\mathrm{Noise_{spec}}}{\sqrt{\mathrm{Num_{fiber}}}}$. For the line width, the uncertainty was based on the correction for instrumental broadening, with the broadening-corrected line considered to have an uncertainty around 10% of the instrumental broadening. The two uncertainties were added in quadrature to determine the final uncertainty on the lines' $\sigma_{\mathrm{H}\alpha}$, with the uncertainty from instrumental broadening dominating.

3.4. Spearman's Rank Correlation Coefficient

Spearman's rank correlation coefficient ρ was used to determine whether the turbulence measures were correlated with star formation activity. ρ is defined as

$$\rho = \frac{\mathrm{cov}(R(X)), \mathrm{cov}(R(Y))}{\sigma_{R(X)}\sigma_{R(Y)}} \quad (7)$$

where cov($R(X)$) and cov($R(Y)$) are the covariances of the rank variables and $\sigma_{R(X)}$ and $\sigma_{R(Y)}$ are standard deviations of the rank variables. Spearman's ρ tests for a monotonic relationship between two variables and does not assume a linear relationship. A value of $\rho \geqslant 0$ indicates a positive correlation, a negative ρ value indicates an anticorrelation, while $\rho = 0$ indicates completely uncorrelated data. $0 < |\rho| < 0.2$ is no correlation, $0.2 < |\rho| < 0.4$ indicates some correlation, $0.4 < |\rho| < 0.7$ indicates a strong correlation, and $0.7 < |\rho| < 1$ indicates a very strong correlation. Along with ρ values, we report the corresponding P-values, or the likelihood of finding the same or more extreme ρ value from a random data set.

4. Ionized Gas Analysis

The results of Spearman's rank correlation tests between the SFR at each time bin and the current Hα velocity dispersion are shown in Figure 6. Each point in Figure 6 demonstrates how correlated the current $\sigma_{\mathrm{H}\alpha}$ is to the SFR at the corresponding time bin. In Figure 6, the strongest peak can be seen at 10–25 Myr timescales. However, as in Hunter et al. (2022), this is not a significant indication of correlation, and is not strong enough to be sufficient evidence of a preferred timescale. Repeated indications of a possible correlation between the current Hα line widths and the SFR 10–25 Myr ago are interesting, as this is at a slightly longer timescale than would be anticipated from the relationship between the Hα-derived SFRs and $\sigma_{\mathrm{H}\alpha}$ found in IFU studies (e.g., Green et al. 2010; Moiseev et al. 2015; Zhou et al. 2017). As the SFHs do not provide the current SFR ($t < 5$ Myr, McQuinn et al. 2010b), we are not sensitive to this previously observed correlation in this analysis. For individual regions, low Hα fluxes would result in very uncertain Hα SFRs and we cannot probe for a correlation on very short timescales. Any selection based on regions with sufficient Hα flux to derive SFRs would be highly biased to recreate previously observed correlations and would ignore the extent of the diffuse ionized gas.

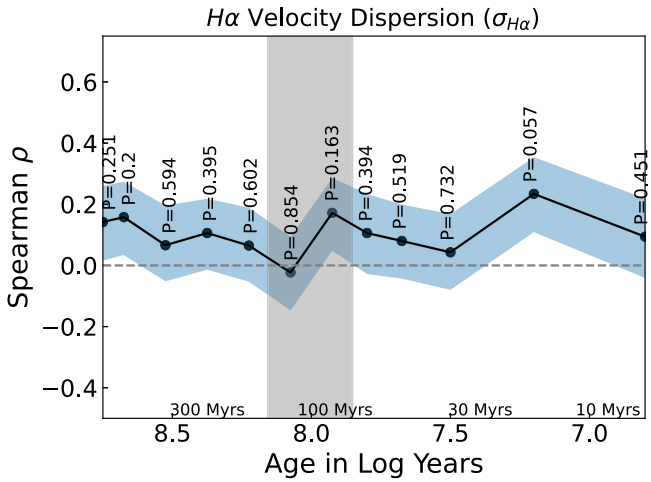

Figure 6. Spearman's correlation coefficient (ρ) vs. log time, or how correlated the star formation rate at a given time is with the Hα velocity dispersion. The 1σ errors based on bootstrapping are the blue shaded region. The associated P-value is listed above each point. For $\sigma_{\mathrm{H}\alpha}$, we find weak evidence of a possible correlation between the velocity dispersion and the SFR in the 10–25 Myr ago bin.

Analysis of the Hα timescales is further complicated by the uneven fiber coverage of the galaxy, with preferential observations of regions with high-surface-brightness Hα emission. Some regions are well filled with fibers covering all, or nearly all, of the area. However, some regions contain as few as one fiber with sufficient signal to noise to be included. This undersampling of some regions results in velocity dispersion measures that only represent a fraction of the area of the region. To determine whether the 10–25 Myr ago timescale correlation exists, a sufficient sample of regions where the majority of fibers have Hα detections is necessary. Thus, further analysis of the Hα timescales will require a larger sample of regions than are provided by a single galaxy. Our planned larger sample of dwarf galaxies will contain enough regions that are well filled with such fibers to determine the validity of this suggested timescale.

5. Results and Discussion: Timescales and Physical Scale of the Atomic Gas

5.1. The 400 pc Scale

Figure 7 shows the analysis of the atomic gas at the 400 pc scale. There is an indication of a 70–140 Myr timescale in Figure 7, looking at both the velocity dispersion and the H I energy surface density. This peak in the correlation coefficient is most prominent at 70–100 Myr for the velocity dispersions and energy surface density measured from the superprofile and at 100–140 Myr for the H I energy surface density measured from the moment map analysis. Thus, it appears the turbulence is not driven by a single prominent burst of star formation, or even the most recent burst of star formation (i.e., the recent uptick at ∼15–30 Myr reported by Weisz et al. 2008; Dalcanton et al. 2012; Cignoni et al. 2018), but by the low constant star formation activity of the past. As previously suggested in Orr et al. (2020), this turbulence driven by older star formation may decay slowly, leaving the impact of past generations observable.

The peak is in agreement with the 100–200 Myr timescales reported in Hunter et al. (2022) based on four galaxies. The

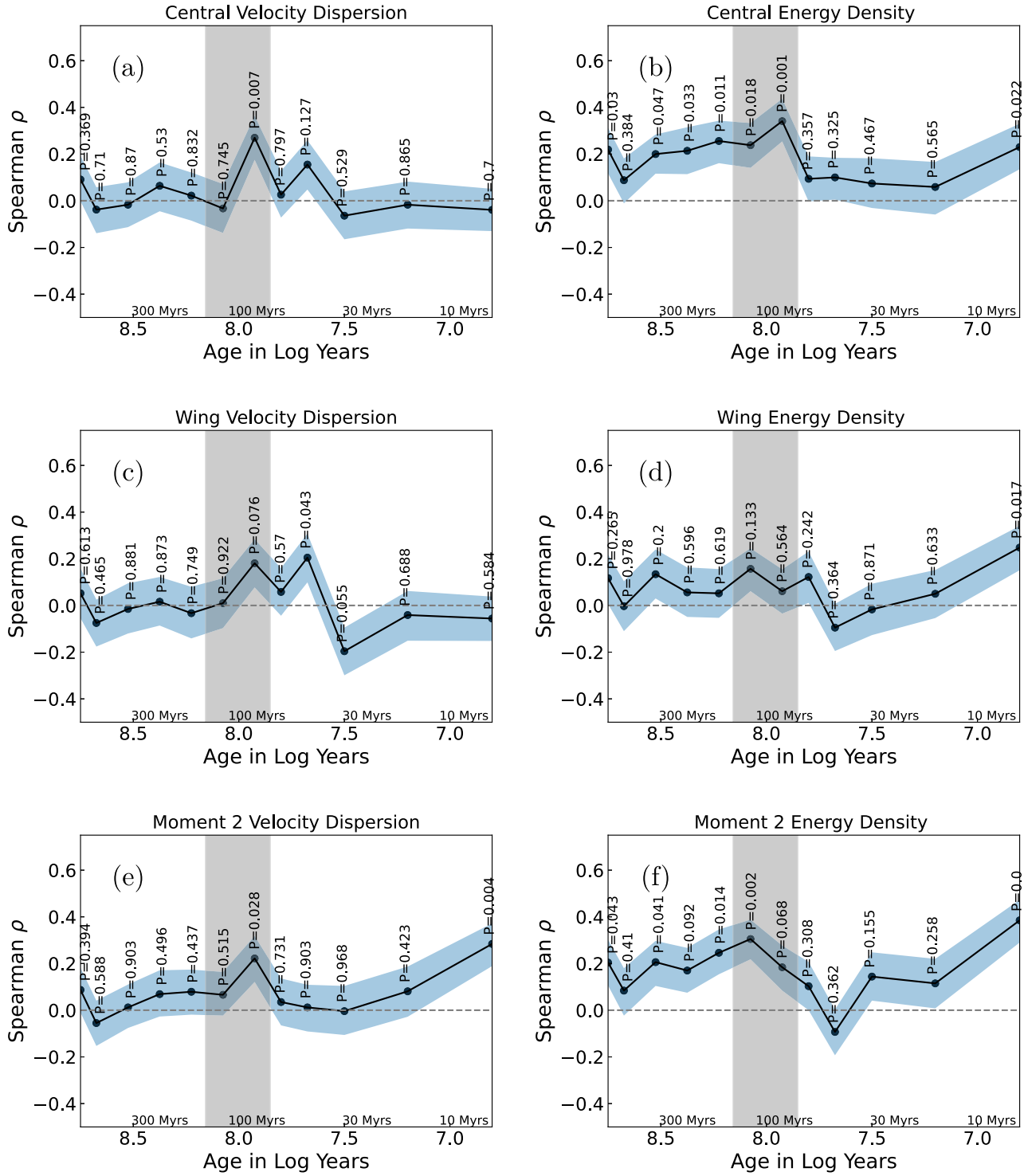

Figure 7. Comparison of H I turbulence measures and SFH on a 400 pc scale: Spearman's correlation coefficient (ρ) vs. log time, or the correlation between a time bin's star formation rate and the H I turbulence measures. The 1σ errors based on bootstrapping are the blue shaded region. The associated P-value is listed above each point. The subfigures are the correlation between the SFH and the velocity dispersion and energy surface density of (a) and (b) the Gaussian superprofile, (c) and (d) the superprofile's wings, and (e) and (f) the second moment map. For the H I turbulence measures in (a), (b), (e), and (f), there is an indication of a correlation with the SFR about 70–140 Myr ago, which is highlighted by the gray shaded region. Additionally, we note the indication of a correlation between the SFR 5–10 Myr ago and the turbulence measures of the second moment map (the rightmost time bin).

slight shift in the timescale may be a product of the difference between UGC 4305 and the previous sample. UGC 4305 has a different geometry to the four previously studied galaxies (NGC 4068, NGC 4163, NGC 6789, and UGC 9128). The previous galaxies are more inclined than UGC 4305; the impact of looking through the disk of the galaxies may have affected the timescale found in Hunter et al. (2022). Significantly inclined galaxies require that we look through the side of the galaxy, and result in a larger three-dimensional volume for a given region. For inclined galaxies, this larger volume would add some uncertainty to the local SFHs and turbulence

measures and may increase the turbulence measures by increasing the rotational broadening.

Additionally, UGC 4305 is larger, with over twice the gas mass and more than 1.5 times the stellar mass of the galaxies in Hunter et al. (2022). Differences in stellar and gas mass and metallicity could also have a noticeable impact on the correlation timescale. Metallicity should impact the correlation timescale because it affects the cooling timescales of the ISM. Such differences in the rate at which thermal energy dissipates could alter what is observed as the correlation timescale for atomic gas turbulence. These differences will be investigated further in a future study of galaxies with a range of physical properties.

The other feature of note is the indication of a correlation at a very short timescale ~5–10 Myr. This is strongest for the energy surface density, which includes the H I surface density, and for the velocity dispersion from the moment maps, which includes a weighting by the H I flux. This peak at the shortest period is likely related to a relationship between atomic gas surface density and SFR surface density for dwarf irregular galaxies (Roychowdhury et al. 2014, 2015). Running Spearman's rank correlation test to compare the current H I mass and the SFR 6–10 Myr ago indicates some positive correlation with $\rho = 0.366$ and $P \leqslant 0.001$.

In Stilp et al. (2013c), a clear correlation between the globally averaged SFR surface density at 30–40 Myr and the H I energy surface density was found. However, as in Hunter et al. (2022), there is no evidence of a 30–40 Myr turbulence timescale in the current analysis. In none of the H I turbulence measures is there evidence of a correlation in the 25–40 Myr time bin (third point from the right in all subfigures of Figure 7). With the lack of an observed 30–40 Myr timescale with the finer ($\Delta\log(t) = 0.15$) time binning (similar to Stilp et al. 2013c's even 10 Myr binning over the past 100 Myr), the difference in observed timescale does not appear to be due to the smearing out of the correlation because of the larger time binning ($\Delta\log(t) = 0.3$) used in Hunter et al. (2022). Instead, the different timescales are likely because there is a physical difference between galaxies' turbulence properties on different scales, and because the timescale of turbulence in the ISM is scale-dependent.

Probing the importance of physical scale in turbulence studies is observationally limited. The 400 pc region size was selected to be large enough to ensure reliable SFHs with sufficient time resolution, and is about the scale height of dwarf galaxy disks (Bacchini et al. 2020). Halving the length of the sides to 200 × 200 pc would run into the resolution of the H I data as the regions would be 12″ × 12″, or approximately the size of the H I beam, barely resolving the H I kinematics. Halving the area would mean 280 × 280 pc or 17″ × 17″, which would not have the H I resolution issue. It would, however, have challenges associated with having enough star counts for reliable SFHs in the outer areas. The limit on SFHs is set by the number of stars within a given region. Significantly decreasing the region size results in much poorer coverage of the galaxy, as only the regions of higher surface brightness can be tested, which disregards much of the H I distributed in the galaxy. Thus, to investigate at smaller scales, deep HST coverage across the entire disk of an extremely nearby galaxy with sufficient recent star formation activity is required. A possible target that fulfills these requirements is M33, and subsequent analysis of these smaller spatial scales may provide further insight.

5.2. 560 and 800 pc Scales

To further probe the physical scale dependence of turbulence, the above analysis was repeated for the atomic gas on sets of larger regions. The region areas were doubled and quadrupled for regions of 560 by 560 pc (34″ a side) and 800 by 800 pc (48″ a side). This re-partition resulted in 49 regions with 560 pc sides and 25 regions with 800 pc sides. When we increased the region size, we reran the SFHs in MATCH for each region using the same method as described in Section 3.1. These SFHs adopted the same time binning of $\Delta\log(t) = 0.15$ over the most recent 560 Myr.

For both the 560 and 800 pc regions, no strong evidence of ~100 Myr or ~40 Myr timescale exists. In Figures 8 and 9, the correlation of the SFH with the H I turbulence measures at different physical scales is shown. The most noteworthy correlation for the larger region sizes is the correlation between H I turbulence measures and the most recent star formation activity, similar to what was seen for the 400 pc regions. As previously discussed, this correlation on the shortest timescales seems to be driven by the correlation between recent star formation activity and the presence of H I gas in dwarf galaxies (Roychowdhury et al. 2014, 2015).

In Figure 8, there are a few peaks in the correlations between the SFH and the H I turbulence; however, these peaks are uncertain as they do not occur for multiple turbulence measures. The strongest peaks are seen in the H I energy surface density from the Gaussian superprofile and the wings, both at 100–140 Myr. However, there do not appear notable peaks for the velocity dispersions or either turbulence measure derived from the moments maps at 100–140 Myr. The indication of a correlation for only two of the six turbulence probes at the same timescale makes the existence of a preferred timescale at the 560 pc scale unclear. For the 800 pc scale (Figure 9) there are no significant correlations between the turbulence measures and the star formation more than 10 Myr ago. There is a peak in the correlation between central energy surface density and the star formation history 25–40 Myr ago in Figure 9 (third time bin from the right) where we would anticipate a correlation based on the result of Stilp et al. (2013a). However, this peak is not significant and does not appear in any other turbulence measure. This leads us to conclude there is no dominant timescale for turbulence on the 560 or 800 pc scale.

The lack of clear indications of a correlation at the ~100 Myr timescale for the larger regions indicates that at the 400 pc scale we are managing to probe the small-scale impact of star formation on the ISM. The majority of H I holes within the HST FoV are on the scale of 19″–30″ diameter (Weisz et al. 2009), which is a scale well matched to our original 400 pc (24″) analysis. Only a few holes are better matched to the increased size of the regions. These larger holes listed in Weisz et al. (2009) and Puche et al. (1992) are better matched to the 560 pc region size than the 800 pc scale. This better scale agreement may be why there are hints of a correlation in the ~100 Myr time bin for the 560 pc regions and not the 800 pc regions. It is clear that larger regions are not as sensitive to the local nature of turbulence driven by supernovae and superbubbles.

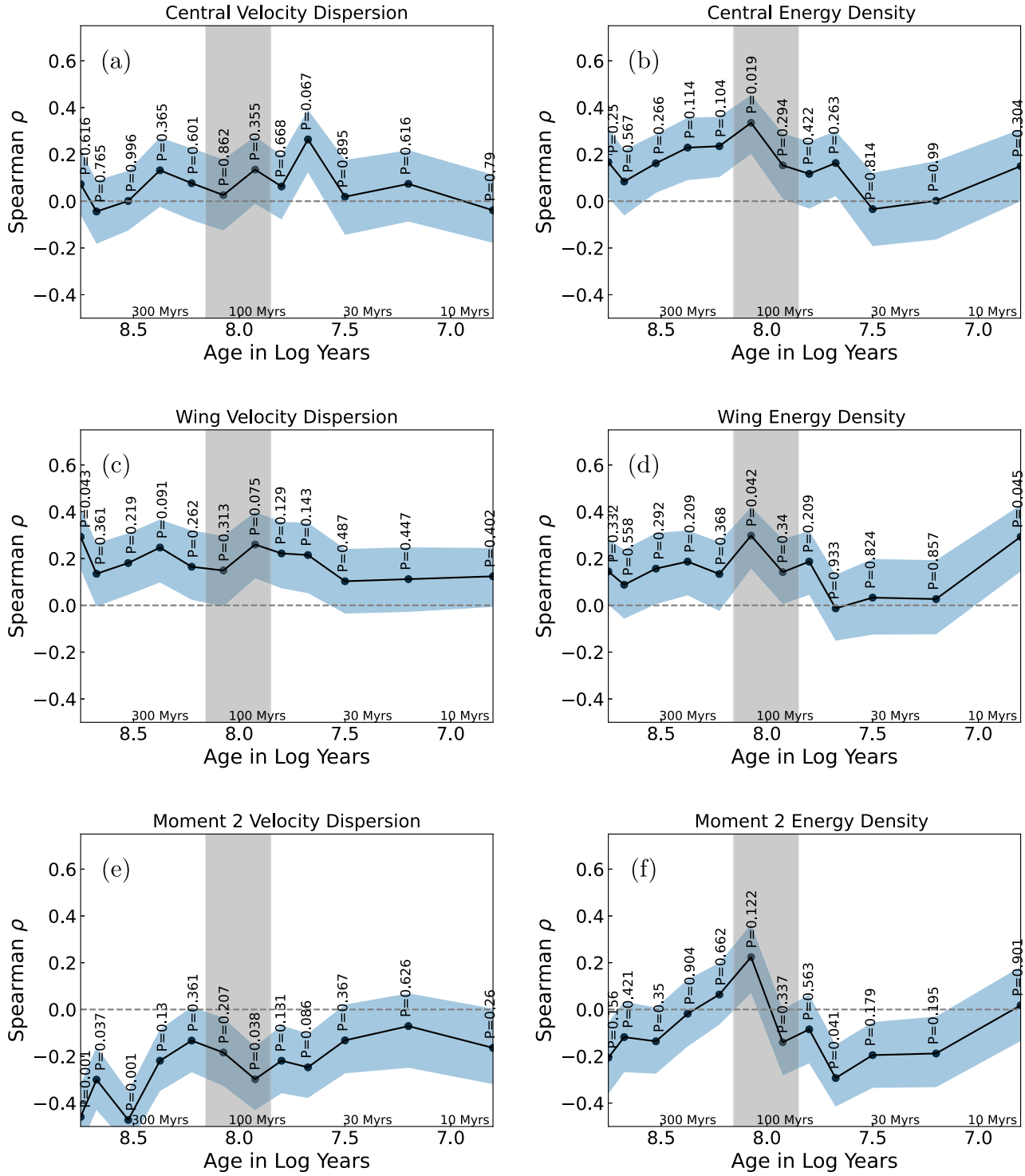

Figure 8. Comparing H I turbulence measures and SFH on a 560 pc scale. As in Figure 7, the subfigures are the correlation between the SFH and the velocity dispersion and energy surface density of (a) and (b) the Gaussian superprofile, (c) and (d) the superprofile's wings, and (e) and (f) the second moment map. For the 560 pc scale, we note a possible correlation between the SFR 5–10 Myr ago and the turbulence measures of the second moment map (the rightmost time bin), and peaks at 100–140 Myr for $\Sigma_{\rm H\,I}$ from the Gaussian superprofile and wings. As in Figure 7, the 70–140 Myr time range is highlighted by the gray shaded region.

The lack of any clear indication of a correlation on the 30–40 Myr timescale for the largest region scale is more surprising. The 800 × 800 pc regions are of a similar size to the areas for five of the 18 galaxies in Stilp et al. (2013c) for their determination of global H I turbulence timescale, but in UGC 4305 these regions are still much smaller than the galaxy. However, Stilp et al. (2013c)'s global analysis included areas from roughly 5.6×10^5 pc^2 to 3.2×10^7 pc^2, covering nearly two orders of magnitude. This combination of multiple physical scales would diminish the importance of a turbulence timescale at a specific physical scale. As such, their results are more sensitive to a general global atomic gas timescale. To have a sufficient sample of regions to determine a turbulence timescale at scales larger than 800 pc would require either

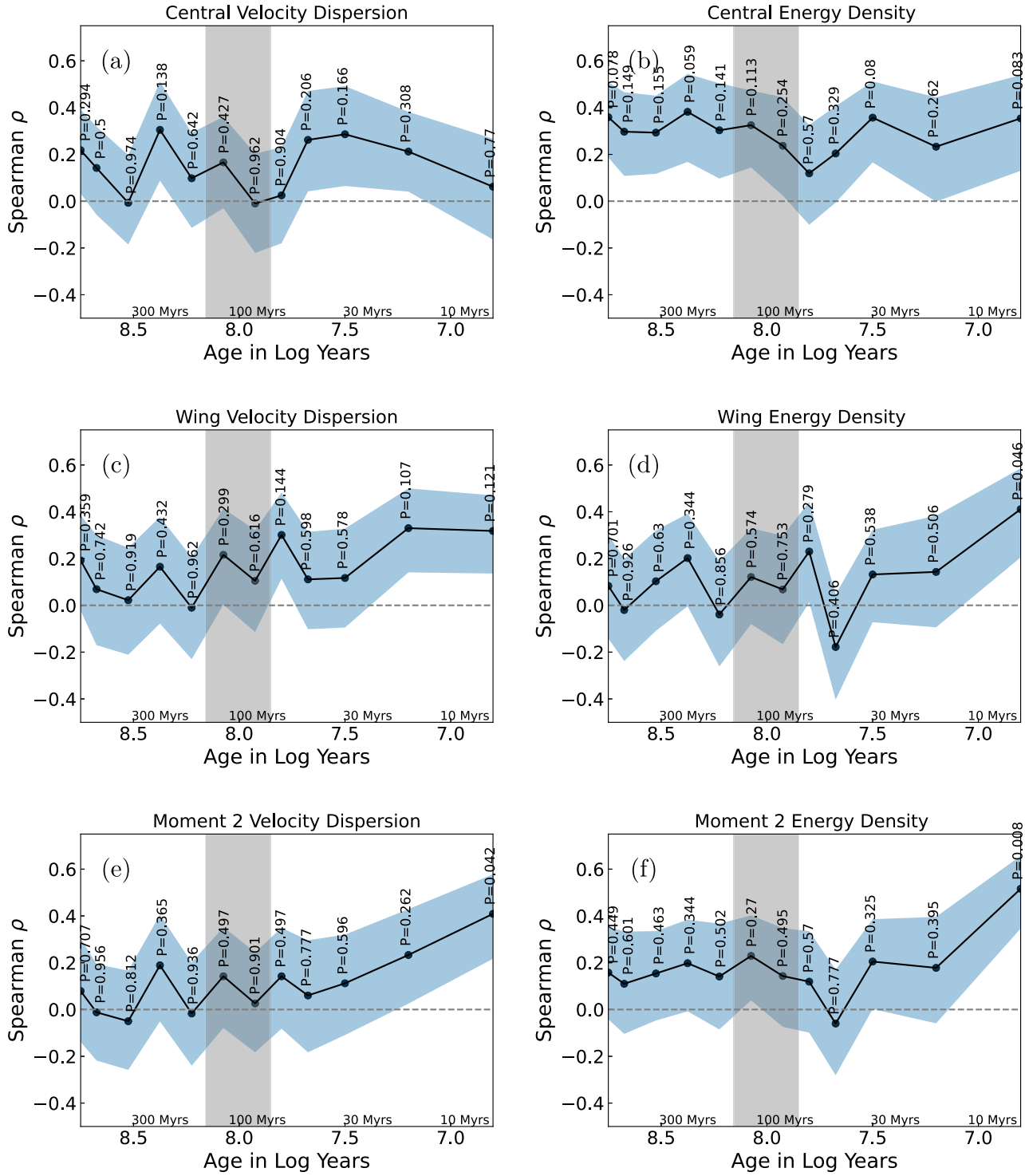

Figure 9. Comparing H I turbulence measures and SFH on a 800 pc scale. As in Figure 7, the subfigures are the correlation between the SFH and the velocity dispersion and energy surface density of (a) and (b) the Gaussian superprofile, (c) and (d) the superprofile's wings, and (e) and (f) the second moment map. For the 800 pc scale the only correlation we note is a possible correlation between the SFR 5–10 Myr ago and the turbulence measures of the second moment map (the rightmost time bin). As in Figure 7, the 70–140 Myr time range is highlighted by the gray shaded region.

switching from the dwarf galaxy regime to spiral galaxies or a sample of larger regions across multiple dwarf galaxies.

6. Conclusions

In this paper, we analyze UGC 4305 using methods outlined in Hunter et al. (2022) on the 400, 560, and 800 pc scales. This analysis utilizes multiwavelength data sets from HST, VLA, and SparsePak (WIYN 3.5 m). We compared the time-resolved SFHs to local H I energy surface density ($\Sigma_{\rm H\,I}$) and velocity dispersion ($\sigma_{\rm H\,I}$), measured from Gaussian fits to H I superprofiles and second moment maps and Hα velocity dispersion using Spearman's rank correlation coefficient.

From the ionized gas, combined with the results from Hunter et al. (2022), we see repeated, but inconclusive evidence of a

correlation between the ionized gas velocity dispersion and the SFR 10–25 Myr ago. For the atomic gas, by analyzing UGC 4305 on multiple physical scales, we probed the importance of physical scale on the turbulence timescale. On the 400 pc scale, there are indications of a correlation between star formation and turbulence in the atomic gas on 70–140 Myr timescales. This correlation timescale is in line with the 100–200 Myr timescale found in Hunter et al. (2022) with an initial sample of four galaxies.

For UGC 4305, the present analysis points to the importance of turbulence and stellar feedback properties on the scale of a few hundred parsecs and in the past ∼150 Myr. A similar ∼100 Myr timescale is part of the discussion of the H I holes and ionized gas shells mapped across the disk of this galaxy (e.g., Puche et al. 1992; Egorov et al. 2017b). While the 70–140 Myr timescale is older than the majority of the dynamical ages of the known H I holes in UGC 4305 (Pokhrel et al. 2020), a relationship between the SFH on similar time and spatial scales (i.e., 100–200 Myr and 250 pc) and the H I kinematics in UGC 4305 was discussed in Weisz et al. (2009). Their work implied that the H I holes in this galaxy were not generated by a series of intense star formation episodes, but by the steady star formation that input energy over time into the ISM over the past 200 Myr. This supports the picture of stellar feedback and its impact on the local atomic gas playing out on a timescale of hundreds of millions of years.

Additionally, we further demonstrated that the difference in the global timescale found in Stilp et al. (2013c) and the local timescale found in Hunter et al. (2022) is more likely driven by a difference in the global and local turbulence properties, not a difference in time resolution. The largest scale regions of 560 and 800 pc did not indicate clearly any preferred timescale for turbulence in UGC 4305. The physical scale-dependent timescale may be related to what drives turbulence at different scales within the ISM.

The results for the three scales presented here (400, 560, and 800 pc) and the global results from Stilp et al. (2013c) demonstrate the complexity of the connection between stellar feedback and turbulence. Together, they indicate that to understand stellar feedback, and its importance in galaxy evolution, both global averages and local ($\leqslant$400 pc) effects must be considered. These observed time delays impact the efficiencies and timescales for propagating star formation in a galaxy.

Further analysis of galaxies at local scales will expand our understanding of the scale dependence of turbulence. A comparison between the correlation timescales of both local and global regions will provide insight into how energy propagates through the ISM and further clarify how turbulence impacts galaxy evolution. As a continuation of this work and Hunter et al. (2022), we are in the process of analyzing the turbulence of dwarf galaxies with a variety of properties. By comparing dwarf galaxies with a variety of properties, our future work will test the range of possible local correlation timescales and provide further insights into the differences between local and global turbulence properties indicated by this work.

Acknowledgments

The anonymous referee is thanked for providing useful, detailed comments on this paper. This work is financially supported through NSF grant Nos. AST-1806522 and AST-1940800. Any opinions, findings, and conclusions or recommendations expressed in this material are those of the authors and do not necessarily reflect the views of the National Science Foundation. Based on observations with the NASA/ESA Hubble Space Telescope obtained from the Data Archive at the Space Telescope Science Institute, which is operated by the Associations of Universities for Research in Astronomy, Incorporated, under NASA contract NAS5-26555. These observations are associated with program No. 10605. Support for program HST-AR-16144 was provided by NASA through a grant from the Space Telescope Science Institute, which is operated by the Associations of Universities for Research in Astronomy, Incorporated, under NASA contract NAS5-26555. Work in this paper was partially supported by NSF REU grant PHY-2150234. Additional support from this work comes from the Indiana Space Grant Consortium Fellowship program and the Indiana University College of Arts and Sciences. The authors acknowledge the observational and technical support from the National Radio Astronomy Observatory (NRAO), and from Kitt Peak National Observatory (KPNO). Observations reported here were obtained with WIYN 3.5 m telescope which is a joint partnership of the NSF's National Optical–Infrared Astronomy Research Laboratory, Indiana University, the University of Wisconsin–Madison, Pennsylvania State University, the University of Missouri, the University of California–Irvine, and Purdue University. This research made use of the NASA Astrophysics Data System Bibliographic Services and the NASA/IPAC Extragalactic Database (NED), which is operated by the Jet Propulsion Laboratory, California Institute of Technology, under contract with the National Aeronautics and Space Administration.

Facility: Hubble Space Telescope; the Very Large Array; the WIYN Observatory.

Software: Astropy (Astropy Collaboration et al. 2013, 2018); GIPSY (van der Hulst et al. 1992); Peak Analysis (Dimeo 2005); IRAF (Tody 1986, 1993).

ORCID iDs

Laura Congreve Hunter https://orcid.org/0000-0001-5368-3632
Kristen B. W. McQuinn https://orcid.org/0000-0001-5538-2614
Andrew E. Dolphin https://orcid.org/0000-0001-8416-4093

References

Aparicio, A., & Hidalgo, S. L. 2009, AJ, 138, 558
Astropy Collaboration, Price-Whelan, A. M., Sipőcz, B. M., et al. 2018, AJ, 156, 123
Astropy Collaboration, Robitaille, T. P., Tollerud, E. J., et al. 2013, A&A, 558, A33
Bacchini, C., Fraternali, F., Pezzulli, G., & Marasco, A. 2020, A&A, 644, A125
Bagetakos, I., Brinks, E., Walter, F., et al. 2011, AJ, 141, 23
Berghea, C. T., Dudik, R. P., Weaver, K. A., & Kallman, T. R. 2010, ApJ, 708, 354
Bernard, E. J., Ferguson, A. M. N., Barker, M. K., et al. 2012, MNRAS, 426, 3490
Bershady, M. A., Andersen, D. R., Harker, J., Ramsey, L. W., & Verheijen, M. A. W. 2004, PASP, 116, 565
Bolatto, A. D., Leroy, A. K., Jameson, K., et al. 2011, ApJ, 741, 12
Bressan, A., Marigo, P., Girardi, L., et al. 2012, MNRAS, 427, 127
Brooks, A. M., Governato, F., Booth, C. M., et al. 2007, ApJL, 655, L17
Bullock, J. S., & Boylan-Kolchin, M. 2017, ARA&A, 55, 343
Bureau, M., & Carignan, C. 2002, AJ, 123, 1316

Christensen, C. R., Davé, R., Brooks, A., Quinn, T., & Shen, S. 2018, ApJ, 867, 142
Cignoni, M., Sacchi, E., Aloisi, A., et al. 2018, ApJ, 856, 62
Croxall, K. V., van Zee, L., Lee, H., et al. 2009, ApJ, 705, 723
Dalcanton, J. J., Williams, B. F., Melbourne, J. L., et al. 2012, ApJS, 198, 6
Dib, S., & Burkert, A. 2005, ApJ, 630, 238
Dimeo, R. 2005, PAN User Guide, NIST ftp://ncnr.nist.gov/pub/staff/dimeo/pandoc.pdf
Dolphin, A. 1997, NewA, 2, 397
DolphinA. (2016) DOLPHOT: Stellar photometry, Astrophysics Source Code Libraryascl:1608.013
Dolphin, A. E. 2000, PASP, 112, 1383
Dolphin, A. E. 2002, MNRAS, 332, 91
Dolphin, A. E. 2013, ApJ, 775, 76
Dolphin, A. E., Weisz, D. R., Skillman, E. D., & Holtzman, J. A. 2005, arXiv: astro-ph/0506430
Egorov, O. V., Lozinskaya, T. A., & Moiseev, A. V. 2017a, MNRAS, 467, L1
Egorov, O. V., Lozinskaya, T. A., Moiseev, A. V., & Shchekinov, Y. A. 2017b, MNRAS, 464, 1833
Elmegreen, B. G., & Scalo, J. 2004, ARA&A, 42, 211
Ford, H. C., Bartko, F., Bely, P. Y., et al. 1998, Proc. SPIE, 3356, 234
Gentry, E. S., Krumholz, M. R., Dekel, A., & Madau, P. 2017, MNRAS, 465, 2471
Green, A. W., Glazebrook, K., McGregor, P. J., et al. 2010, Natur, 467, 684
Harris, J., & Zaritsky, D. 2001, ApJS, 136, 25
Hodge, P., Strobel, N. V., & Kennicutt, R. C. 1994, PASP, 106, 309
Holtzman, J. A., Gallagher, John, S., & Cole, I. 1999, AJ, 118, 2262
Hunter, D. A., Elmegreen, B. G., Archer, H., Simpson, C. E., & Cigan, P. 2021, AJ, 161, 175
Hunter, D. A., Hawley, W. N., & Gallagher, J. S. I. 1993, AJ, 106, 1797
Hunter, L. C., van Zee, L., McQuinn, K. B. W., Garner, R., & Dolphin, A. E. 2022, AJ, 163, 132
Ianjamasimanana, R., de Blok, W. J. G., Walter, F., & Heald, G. H. 2012, AJ, 144, 96
Joung, M. R., Mac Low, M.-M., & Bryan, G. L. 2009, ApJ, 704, 137
Kaaret, P., Ward, M. J., & Zezas, A. 2004, MNRAS, 351, L83
Kennicutt, R. C., & Evans, N. J. 2012, ARA&A, 50, 531
Kim, C.-G., Ostriker, E. C., & Raileanu, R. 2017, ApJ, 834, 25
Kroupa, P. 2001, MNRAS, 322, 231
Mac Low, M.-M., & Klessen, R. S. 2004, RvMP, 76, 125
McQuinn, K. B. W., Mitchell, N. P., & Skillman, E. D. 2015, ApJS, 218, 29
McQuinn, K. B. W., Skillman, E. D., Cannon, J. M., et al. 2010a, ApJ, 721, 297
McQuinn, K. B. W., Skillman, E. D., Cannon, J. M., et al. 2010b, ApJ, 724, 49
McQuinn, K. B. W., van Zee, L., & Skillman, E. D. 2019, ApJ, 886, 74
Miller, N. A., Mushotzky, R. F., & Neff, S. G. 2005, ApJL, 623, L109
Moiseev, A. V., Tikhonov, A. V., & Klypin, A. 2015, MNRAS, 449, 3568
Moran, E. C., Halpern, J. P., & Helfand, D. J. 1996, ApJS, 106, 341
Orr, M. E., Hayward, C. C., Medling, A. M., et al. 2020, MNRAS, 496, 1620
Pokhrel, N. R., Simpson, C. E., & Bagetakos, I. 2020, AJ, 160, 66
Puche, D., Westpfahl, D., Brinks, E., & Roy, J.-R. 1992, AJ, 103, 1841
Rhode, K. L., Salzer, J. J., Westpfahl, D. J., & Radice, L. A. 1999, AJ, 118, 323
Roychowdhury, S., Chengalur, J. N., Kaisin, S. S., & Karachentsev, I. D. 2014, MNRAS, 445, 1392
Roychowdhury, S., Huang, M.-L., Kauffmann, G., Wang, J., & Chengalur, J. N. 2015, MNRAS, 449, 3700
Schlafly, E. F., & Finkbeiner, D. P. 2011, ApJ, 737, 103
Schlegel, D. J., Finkbeiner, D. P., & Davis, M. 1998, ApJ, 500, 525
Spitzer, L. 1978, Physical Processes in the Interstellar Medium (New York: Wiley)
Stewart, S. G., Fanelli, M. N., Byrd, G. G., et al. 2000, ApJ, 529, 201
Stilp, A. M., Dalcanton, J. J., Skillman, E., et al. 2013a, ApJ, 773, 88
Stilp, A. M., Dalcanton, J. J., Warren, S. R., et al. 2013b, ApJ, 765, 136
Stilp, A. M., Dalcanton, J. J., Warren, S. R., et al. 2013c, ApJ, 772, 124
Tamburro, D., Rix, H. W., Leroy, A. K., et al. 2009, AJ, 137, 4424
Tody, D. 1986, Proc. SPIE, 627, 733
Tody, D. 1993, in ASP Conf. Ser. 52, Astronomical Data Analysis Software and Systems II, ed. R. J. Hanisch, R. J. V. Brissenden, & J. Barnes (San Francisco, CA: ASP), 173
Tolstoy, E., & Saha, A. 1996, ApJ, 462, 672
Tremonti, C. A., Heckman, T. M., Kauffmann, G., et al. 2004, ApJ, 613, 898
Tully, R. B., Courtois, H. M., Dolphin, A. E., et al. 2013, AJ, 146, 86
van der Hulst, J. M., Terlouw, J. P., Begeman, K. G., Zwitser, W., & Roelfsema, P. R. 1992, in ASP Conf. Ser. 25, Astronomical Data Analysis Software and Systems I, ed. D. M. Worrall, C. Biemesderfer, & J. Barnes (San Francisco, CA: ASP), 131
van Zee, L., Maddalena, R. J., Haynes, M. P., Hogg, D. E., & Roberts, M. S. 1997, AJ, 113, 1638
Warren, S. R., Skillman, E. D., Stilp, A. M., et al. 2012, ApJ, 757, 84
Weisz, D. R., Dalcanton, J. J., Williams, B. F., et al. 2011, ApJ, 739, 5
Weisz, D. R., Dolphin, A. E., Skillman, E. D., et al. 2014, ApJ, 789, 147
Weisz, D. R., Skillman, E. D., Cannon, J. M., et al. 2008, ApJ, 689, 160
Weisz, D. R., Skillman, E. D., Cannon, J. M., et al. 2009, ApJ, 704, 1538
Young, L. M., van Zee, L., Lo, K. Y., Dohm-Palmer, R. C., & Beierle, M. E. 2003, ApJ, 592, 111
Yu, X., Shi, Y., Chen, Y., et al. 2019, MNRAS, 486, 4463
Zezas, A. L., Georgantopoulos, I., & Ward, M. J. 1999, MNRAS, 308, 302
Zhou, L., Federrath, C., Yuan, T., et al. 2017, MNRAS, 470, 4573